RSC Advances

ROYAL SOCIETY OF CHEMISTRY

PAPER

View Article Online
View Journal | View Issue

Check for updates

Cite this: *RSC Adv.*, 2022, **12**, 18994

Quantum chemical study of the reaction paths and kinetics of acetaldehyde formation on a methanol–water ice model†

Islem Ben Chouikha, *[a] Boutheïna Kerkeni, *[ab] Ghofrane Ouerfelli,[ac] Lily Makroni[d] and Gunnar Nyman*[e]

Received 8th June 2022
Accepted 15th June 2022

DOI: 10.1039/d2ra03555c

rsc.li/rsc-advances

Acetaldehyde (CH_3CHO) is ubiquitous in interstellar space and is important for astrochemistry as it can contribute to the formation of amino acids through reaction with nitrogen containing chemical species. Quantum chemical and reaction kinetics studies are reported for acetaldehyde formation from the chemical reaction of C(^{3}P) with a methanol molecule adsorbed at the eighth position of a cubic water cluster. We present extensive quantum chemical calculations for total spin $S = 1$ and $S = 0$. The UωB97XD/6-311++G(2d,p) model chemistry is employed to optimize the structures, compute minimum energy paths and zero-point vibrational energies of all reaction steps. For the optimized structures, the calculated energies are refined by CCSD(T) single point computations. We identify four transition states on the triplet potential energy surface (PES), and one on the singlet PES. The reaction mechanism involves the intermediate formation of CH_3OCH adsorbed on the ice cluster. The rate limiting step for forming acetaldehyde is the C–O bond breaking in CH_3OCH to form adsorbed CH_3 and HCO. We find two positions on the reaction path where spin crossing may be possible such that acetaldehyde can form in its singlet spin state. Using variational transition-state theory with multidimensional tunnelling we provide thermal rate constants for the energetically rate limiting step for both spin states and discuss two routes to acetaldehyde formation. As expected, quantum effects are important at low temperatures.

1 Introduction

The complexity of the chemical networks that take part in the formation and fragmentation processes of interstellar species depend on the physical evolution of the star-formation cycles, such as changes in density, temperature, and spectral shape and intensity of radiation.[1] The synthesis of interstellar species occurs in some cases on surfaces of grains, or *via* gas phase reactions, and in some other cases as a combination of these. Knowledge of the pathways that lead to the synthesis of organic molecules in space could help in understanding if such chemistry could lead to the emergence of life on Earth.[2]

The search for the chemical routes leading to the formation of interstellar Complex Organic Molecules (COMs), *viz.* organic species with six or more atoms,[3,4] has motivated several research groups to investigate them theoretically,[5–11] observationally,[1,12] and experimentally.[13–15] In particular, acetaldehyde (CH_3CHO) was first detected in 1973 (ref. 16) and plays a key role in the chemistry of the Interstellar Medium (ISM).[17] Astronomical observations toward cold and dark clouds in star-forming regions show the abundance of acetaldehyde to be approximately $\sim 10^{-10}$ to 10^{-9} with respect to the density of H_2.[18–20] Acetaldehyde has been observed in the gas phase toward several environments such as translucent clouds,[21] pre-stellar cores,[22] the comet Hale–Bopp[23] but also in interstellar ices[6,7,24] and meteorites.[25]

Acetaldehyde is the simplest methyl-bearing aldehyde and constitutes a critical precursor to prebiotic molecules such as glycolaldehyde (CH_2OHCHO)[26] and acrolein (CH_2CHCHO). The latter is a crucial intermediate in the prebiotic synthesis of various amino acids[27] and plays an important role in astrobiology.[28] For these reasons, CH_3CHO is one of the most studied molecules in the ISM in recent years.

So far, formation of acetaldehyde has been investigated in the gas phase,[29,30] on pure water ice models,[31–33] ice containing

---

[a] Département de Physique, LPMC, Faculté des Sciences de Tunis, Université de Tunis el Manar, Tunis 2092, Tunisia. E-mail: islem.benchouikha@fst.utm.tn
[b] ISAMM, Université de la Manouba, La Manouba 2010, Tunisia. E-mail: boutheina.kerkeni@isamm.uma.tn
[c] Taif University, Taif, Saudi Arabia
[d] Key Laboratory for Macromolecular Science of Shaanxi Province, School of Chemistry and Chemical Engineering, Shaanxi Normal University, Xi'an, Shaanxi, 710119, China
[e] Department of Chemistry and Molecular Biology, University of Gothenburg, Sweden. E-mail: nyman@chem.gu.se

† Electronic supplementary information (ESI) available: The following files are available free of charge, COORD: ASCII files for all XYZ coordinates pertaining to I_1, I_2, P_1, P_2, P_3, TS1, TS2, TS3 and TS4 for possible spin states $S = 0$, 1. This material is available free of charge *via* the Internet at https://pubs.acs.org/. See https://doi.org/10.1039/d2ra03555c

methanol,[34] and on amorphous CO-rich ice cluster models.[6,7,35,36] Quantum chemical calculations on the formation of CH_3CHO from the reaction between HCO and CH_3 radicals have been performed by Enrique-Romero *et al.*[31] The broken symmetry (BS) approach was not initially considered in their DFT calculations, and only CH_4 + CO can be formed on an amorphous molecular water ice cluster. In gas phase, possible spontaneous products are CH_3CHO, CH_4 + CO, and CH_3OCH depending on the initial orientation of the reagents.[31] The gas phase formation of CH_3CHO and CH_3OCH however requires a third body or spontaneous emission of a photon in order to stabilize the molecules. These conclusions have been revoked later by Enrique-Romero *et al.*,[33] when an unrestricted BS approach was employed. As a consequence, the authors report that in gas phase the CH_3CHO and CH_4 + CO channels are barrierless, while CH_3OCH presents a high barrier. In contrast, on an ice model represented by a single H_2O molecule, H transfer from HCO to CH_3 to form CH_4 + CO presented a very high barrier, while the formation of CH_3CHO was found to be barrierless, as in the gas phase. Other calculations on two model clusters comprised of 18 and 33 water molecules reported similar findings.[32]

Synthesis of acetaldehyde in the gas phase has been studied through several mechanisms using the KIDA[37] and UDfA[38] databases.

None of these appear to yield sufficient acetaldehyde to explain its interstellar abundance and Vazart and co-workers[5] wrote a critical review of the gas-phase formation routes of acetaldehyde invoked in the literature. The prevailing theory of the formation of COMs relies on their chemistry at the surface of warm grains. Acetaldehyde has, however, been observed at very low temperatures, hence challenging the warm scenario.

Bennett and co-workers[6,7] studied synthetic routes toward acetaldehyde formation inside ice mixtures of carbon monoxide and methanol condensed at 10 K from both experimental and computational points of view.

These and other laboratory experiments provide compelling evidence that acetaldehyde can easily form in interstellar ices containing carbon monoxide and methane,[6,7,35] methanol,[34] ethane (CH_3CH_3) or ethylene (CH_2CH_2),[39] and pure methanol ices,[40] or by oxidation of ethanol (CH_3CH_2OH)[41]/2-propanol ($CH_3CH_2OHCH_3$)[42,43] when exposed to ionizing radiation.[42]

In this article, we focus on a solid-state chemistry formation mechanism that has been proposed in the literature.[44] We perform new electronic structure calculations on the energetics of this mechanism. Our main purpose is to investigate the role of the spin and calculate thermal rate constants for the rate limiting step of the proposed mechanism. This information can then be used in astrochemical modelling.

We study the formation of acetaldehyde following the Eley-Rideal mechanism where gas phase $C(^3P)$ approaches a methanol molecule which is part of a model grain also composed of 7 water molecules.

The overall reaction is:

$$C(^3P)(gas) + {}^1CH_3OH\text{-}7w(cluster) \rightarrow {}^1CH_3CHO(gas) + {}^17w(cluster),$$

where 7w(cluster) stands for a cluster of 7 water molecules.

Singh *et al.*[44] proposed, where we below essentially use their notation, some (involving only total spin $S = 1$) of the following elementary steps:

Step 1: RC → I_1

$$C(^3P)(gas) + {}^1CH_3OH\text{-}7w(cluster) \rightarrow {}^3CH_3OHC(ads)\text{-}7w(cluster)$$

Step 2: I_1 → I_2

$${}^3CH_3OHC(ads)\text{-}7w(cluster) \rightarrow {}^3CH_3OCH(ads)\text{-}7w(cluster)$$

We also consider intersystem crossing and investigate formation of $^1CH_3OCH$(ads)-7w(cluster) in Step 2. Consequently, the Step 3 below has also been studied on the singlet spin potential energy surface in this paper.

Step 3: I_2 → P_1

$${}^3CH_3OCH(ads)\text{-}7w(cluster) \rightarrow {}^3[CH_3 + HCO](ads)\text{-}7w(cluster)$$

or

I_2 → P_1

$${}^1CH_3OCH(ads)\text{-}7w(cluster) \rightarrow {}^1[CH_3 + HCO](ads)\text{-}7w(cluster)$$

Step 4: P_1 → P_2

$${}^1[CH_3 + HCO](ads)\text{-}7w(cluster) \rightarrow {}^1CH_3CHO(ads)\text{-}7w(cluster).$$

or

$${}^3[CH_3 + HCO](ads)\text{-}7w(cluster) \rightarrow {}^3CH_3CHO(ads)\text{-}7w(cluster).$$

We will additionally comment on:

Step 4′: P_1 → P_3

$${}^1[CH_3 + HCO](ads)\text{-}7w(cluster) \rightarrow {}^1[CH_4(ads) + CO](ads)\text{-}7w(cluster).$$

and

$${}^3[CH_3 + HCO](ads)\text{-}7w(cluster) \rightarrow {}^3[CH_4(ads) + CO](ads)\text{-}7w(cluster).$$

In Section 2 we describe the adopted computational methods for electronic structure and rate constants calculations and in Section 3 we discuss the results and their implications. Finally conclusions are given in Section 4.

2 Methodology

In the present work we employ density functional theory (DFT),[45] and CCSD(T)[46] to investigate acetaldehyde (Ac) formation on a model grain comprised of seven water molecules and a single methanol molecule that substitutes the 8th water molecule of a cubic cluster.

All quantum chemical calculations have been performed with the Gaussian 16 software.[47]

2.1 Density functional theory (DFT) calculations

In our work all structures are fully optimized and the harmonic frequencies computed using DFT. Frequency calculations were performed in order to verify that all intermediates are true minima on the potential energy surface, and that all transition states exhibit a single imaginary frequency.

We use the range separated UωB97XD hybrid meta-GGA exchange–correlation functional[48] with its dispersion corrections which yields satisfactory accuracy for the thermochemistry, kinetics, and non-covalent interactions. Thus, it can be used to study our model system and describes accurately the interactions that play an important role in the stability of the different fragments involved in the reaction process leading to acetaldehyde.[48]

The split valence triple ζ Pople basis set 6-311++G(2d,p)[49] includes polarisation and diffuse functions and is able to describe van der Waals interactions inside the ice model and molecular interactions with the fragments. Further, this basis set is shown to provide near experimental accuracy for many chemical reactions.[50,51] We study all species in the reaction mechanism with the UωB97XD/6-311++G(2d,p) model chemistry. Gaussian 16 automatically includes an ultrafine integration grid in the DFT calculations in order to improve the accuracy of the results. The grid greatly enhances the accuracy at reasonable additional cost.

The reaction paths are computed using the intrinsic reaction coordinate (IRC) methodology[52,53] to confirm the identities of the reactants and products for every transition state.

IRC calculations require initial force constants of the transition state. Then, the first and second order energy derivatives are obtained to calculate the projected harmonic vibrational frequencies along each reaction path. The Minimum Energy Paths (MEPs) for Steps 2, 3 and 4 were computed using the Page–McIver integrator with a gradient step size of 0.1 a_0.

2.2 Coupled cluster calculations

In order to better describe the energetics, single point energy calculations were performed for all involved species using CCSD(T)[46] on the DFT optimized geometries.

As the calculations become time intensive for larger basis set choices, the same basis set was used as in the DFT calculations and this composite method will in the following be referred to as CCSD(T)//UωB97XD/6-311++G(2d,p).

2.3 Semi-classical theory of the rate constants

Rate constants for Step 3 (for both spin states $S = 0, 1$) in the reaction mechanism, which is energetically rate limiting, are computed over the temperature range [105–2000 K] with the general polyatomic rate constant code POLYRATE version 2010-A.[54] Transition state theory is employed in various forms as described below.

The connectivity between a transition state and the desired reactant or product is verified by performing intrinsic reaction coordinate calculations in both the forward and backward directions with a step size of 0.1 Bohr.

Conventional transition state theory. The conventional transition-state-theory rate constant, $k_{\mathrm{TST}}(T)$, is given by the following expression for uni-molecular reactions:[55]

$$k_{\mathrm{TST}}(T) = \sigma \frac{k_{\mathrm{B}} T}{h} \frac{Q_{\mathrm{elec}}^{\mathrm{TS}} Q_{\mathrm{rot}}^{\mathrm{TS}}(T) Q_{\mathrm{vib}}^{\mathrm{TS}}(T)}{Q_{\mathrm{elec}}^{\mathrm{R}} Q_{\mathrm{rot}}^{\mathrm{R}}(T) Q_{\mathrm{vib}}^{\mathrm{R}}(T)} \times \exp\left[-\frac{E_{\mathrm{TS}} - E_{\mathrm{reactant}}}{k_{\mathrm{B}} T}\right], \tag{1}$$

where $E_{\mathrm{TS}} - E_{\mathrm{Reactant}} = \Delta V$ is the classical barrier height, σ represents the symmetry number referring to reaction path degeneracy, h is Planck's constant, and k_{B} is the Boltzmann constant. Q^{TS} and Q^{R} are the transition state (TS) and reactant (R) partition functions, respectively, which can be expressed as a product of the partition functions of the internal motions (vibration, rotation), and the electronic distribution. Rotational partition functions are calculated classically within the rigid rotor harmonic oscillator approximation and the vibrational partition functions are calculated as separable quantum mechanical harmonic oscillators. σ is always unity in the present work.

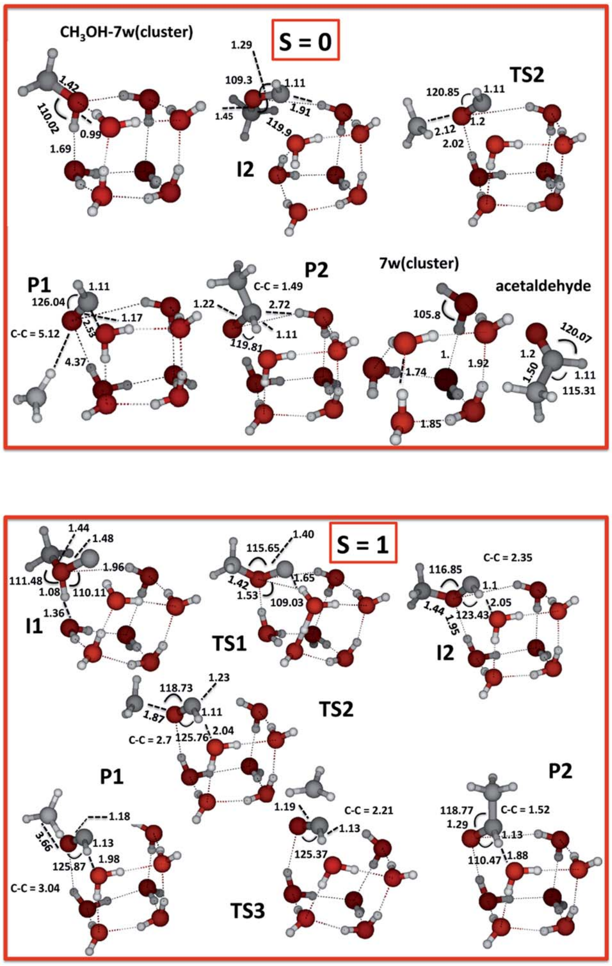

Fig. 1 Fully optimised final geometries for all reactants, and complexes computed with UωB97XD/6-311++G(2d,p) for the two spin states $S = 0$ and 1.

Canonical variational transition state theory. Canonical variational transition-state theory (CVT)[56] has been used to estimate the rate constants. The canonical variational, transition state theory rate constant k_{CVT} is obtained by finding the location of the minimum flux through the transition state at a given temperature.

Note that in using a free energy of activation criterion to determine the location of the variational transition state, both entropic and energetic contributions are taken into account. We may write:

$$k_{\mathrm{CVT}}(T) = \min_s k^{\mathrm{G}}(T,s) = k^{\mathrm{G}}(T,s^{\star,\mathrm{CVT}}(T)), \tag{2}$$

where

$$k^{\mathrm{G}}(T,s) = \sigma \frac{k_{\mathrm{B}}T}{h} \frac{Q^{\mathrm{TS}}(T,s)}{Q^{\mathrm{R}}(T)} \exp\left[-\frac{V_{\mathrm{MEP}}(s)}{k_{\mathrm{B}}T}\right]. \tag{3}$$

Here $V_{\mathrm{MEP}}(s)$ is the classical potential along the minimum energy path referenced to the reactant energy, s is the mass scaled reaction coordinate and $s^{\star,\mathrm{CVT}}$ is the location of the canonical transition state on the reaction path, *i.e.* where the flux is minimal.

$s = 0$ at the transition state, at the reactants it is a finite negative number, and for the products a finite positive number.

Zero curvature tunneling (ZCT) method. When the reaction path curvature can be neglected, the proper tunneling path is the MEP. For tunneling along the MEP, $\theta(E)$ is used to describe the imaginary action integral given by

$$\theta(E) = \hbar^{-1} \int_{s_0}^{s_1} \mathrm{d}s \left[2\mu\left[V_{\mathrm{a}}^{\mathrm{G}}(s) - E\right]\right]^{1/2}, \tag{4}$$

where $V_{\mathrm{a}}^{\mathrm{G}}(s) = V_{\mathrm{MEP}}(s) + \mathrm{ZPE}(s)$, and ZPE is the zero point energy corresponding to the frequencies orthogonal to the reaction path.

A tunnelling probability is calculated as

$$P(E) = \exp[-2\theta(E)], \tag{5}$$

which can be used to obtain a transmission coefficient $\kappa(T)$ from,

$$\kappa(T) = \frac{\int_0^{\infty} P(E)\exp\left(-\dfrac{E}{k_{\mathrm{B}}T}\right)\mathrm{d}E}{\int_{V_{\mathrm{a}}^{\mathrm{G}}(s=0)}^{\infty} \exp\left(-\dfrac{E}{k_{\mathrm{B}}T}\right)\mathrm{d}E}. \tag{6}$$

This $\kappa(T)$ multiplies the otherwise obtained thermal rate constant to give a tunnelling corrected rate constant,

$$k_{\mathrm{ZCT}}(T) = \kappa(T) \times k_{\mathrm{TST}}(T). \tag{7}$$

This approach is called the zero curvature tunneling (ZCT) method.[57]

Small curvature tunneling (SCT) method. Liu *et al.*[56] have reported that tunnelling probabilities may increase because of the so called corner-cutting effect, which is not accounted for in the ZCT method. More advanced tunneling methods are based on the inclusion of deviations between the tunneling path and the minimum energy path.[58]

In the small curvature tunneling method (SCT),[56] transmission coefficients,[57,59] which include effects of the reaction-path curvature, are based on the centrifugal-dominant small-curvature semi-classical adiabatic ground-state (CD-SCSAG)

Table 1 Energies (in Hartree) for a total spin $S = 0$ and 1 computed at UωB97XD/6-311++G(2d,p) and CCSD(T)//UωB97XD/6-311++G(2d,p) levels and zero point energies at UωB97XD/6-311++G(2d,p) level for all species involved along the reaction path

Species	Energy (UωB97XD)	ZPE (UωB97XD)	Energy + ZPE (UωB97XD)	Energy CCSD(T)//UωB97XD	Energy + ZPE CCSD(T)//UωB97XD
$S = 1$					
C(^{3}P)	−37.840178	—	−37.840178	−37.773973	−37.773973
I_1	−688.780084	0.236295	−688.543789	−687.548089	−687.311794
TS1	−688.777331	0.230375	−688.546956	−687.541491	−687.311116
I_2	−688.828564	0.235519	−688.593045	−687.595794	−687.360275
TS2	−688.801766	0.230675	−688.571091	−687.569784	−687.339109
P_1	−688.837208	0.227453	−688.609755	−687.609865	−687.382412
TS3	−688.834115	0.230081	−688.604034	−687.601360	−687.371279
P_2	−688.862109	0.234261	−688.627848	−687.623084	−687.388823
TS4	−688.790605	0.228354	−688.562251	−687.551798	−687.323444
P_3	−688.807343	0.233586	−688.573757	−687.571456	−687.337870
CH_3CHO(gas)	−153.709122	0.052916	−153.656206	−153.399772	−153.346856
$S = 0$					
Ice model: CH_3OH-7w	−650.894314	0.235504	−650.658810	−649.742209	−649.506705
7w(cluster)	−535.138321	0.179647	−534.958674	−534.211967	−534.032320
I_2	−688.875062	0.237861	−688.637201	−687.644363	−687.406502
TS2	−688.827359	0.229755	−688.597604	−687.597604	−687.368810
P_1	−688.837677	0.227578	−688.610099	−687.610245	−687.382667
P_2	−688.982611	0.237554	−688.745056	−687.750202	−687.512648
P_3	−688.973831	0.232680	−688.741151	−687.755034	−687.522354
CH_3CHO(gas)	−153.829051	0.055686	−153.773365	−153.523343	−153.467657

approximation.[56] The SCT method is known to predict reasonably accurate rate constants[60–62] and is therefore widely used.

In the SCT method the effect of the reaction curvature is included by replacing the reduced mass μ by an effective mass μ_{eff}. The tunnelling probability at energy E is

$$P(E) = \frac{1}{1 + \mathrm{e}^{-2\theta(E)}} \tag{8}$$

where $\theta(E)$ is the imaginary action integral along the tunnelling path

$$\theta(E) = \hbar^{-1}\int_{s_0}^{s_1} \mathrm{d}s\left\{2\mu_{\text{eff}}\left[V_\mathrm{a}^\mathrm{G} - E\right]\right\}^{1/2}. \tag{9}$$

$\kappa(T)$ is calculated as in eqn (4) and the thermal rate constant is tunnelling corrected in the corresponding way as done for ZCT. Details of the theory can be found in ref. 63.

3 Results and discussion

In this section we first report our electronic structure calculations and then the rate constants that we have obtained for the energetically rate determining step, Step 3, on both the singlet and triplet potential energy surfaces.

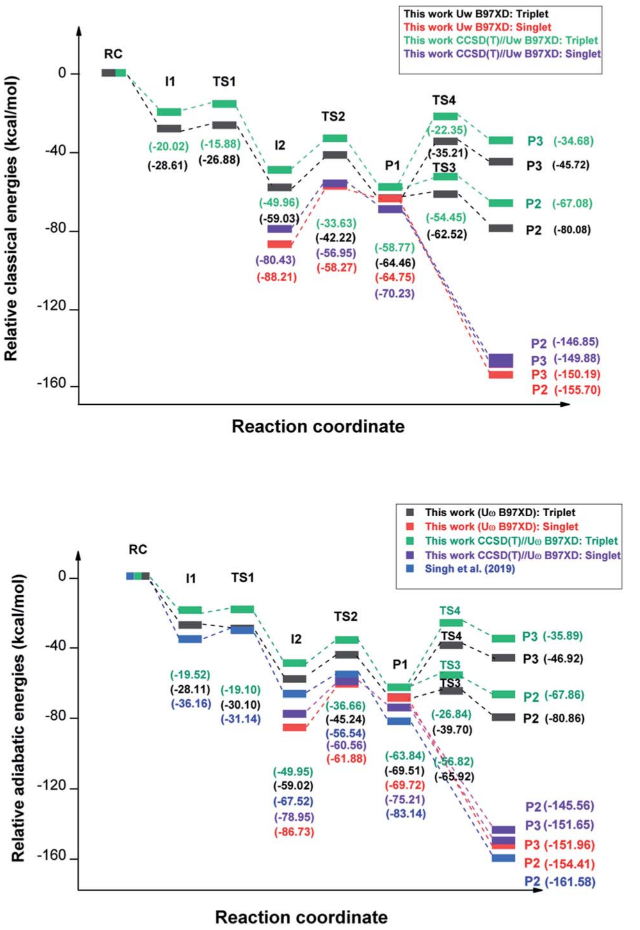

Fig. 2 Schematic potential energy surfaces for the complete reaction mechanism computed with UωB97XD/6-311++G(2d,p) and CCSD(T)//UωB97XD. Relative classical (top) and adiabatic (bottom) energies are compared to those from ref. 44 (blue lines). We plot our calculated values for the two spin states $S = 0$ (red and purple lines) and $S = 1$ (black and green lines).

3.1 Electronic structure calculations

From the electronic structure calculations we computed intermediates, transition states and products as illustrated in Fig. 1 for the singlet and triplet species.

All structures are optimised at the UωB97XD/6-311++G(2d,p) level. Transition states correspond to the first-order saddle points characterized by single imaginary frequencies. For the triplet species these frequencies are $758i$ cm^{-1} for the H atom transfer in Step 2, $762i$ cm^{-1} for the C–O bond breakage in Step 3, $243i$ cm^{-1} for the C–C bond formation in Step 4, and $1445i$ cm^{-1} for the H abstraction in Step 4′.

As the carbon atom approaches the CH_3OH–water complex, the formation of intermediate I_1 occurs without a barrier (Step 1). This is followed by hydrogen transfer from the oxygen atom of methanol to the carbon atom *via* a proton relay-mechanism involving the water molecules of the ice model through the transition state TS1, to yield a more stable intermediate I_2 (Step 2). Another barrier-mediated (TS2) step generates the adsorbed radicals CH_3 and HCO, *i.e.* the P_1 complex (Step 3). These first three steps may occur on the triplet PES. Spin flip could however take place close to the intermediate I_2 ($S = 1$), thereby yielding I_2 ($S = 0$). This would allow the reaction to continue on the singlet PES, see more below. In Step 4 acetaldehyde adsorbed on the ice (P_2) forms.

We have computed the possible fragments on the singlet ($S = 0$) PES employing "Stable = Opt" first to ensure that we get the lowest singlet SCF solution, as we are interested in finding an SCF solution of an open shell unrestricted singlet wavefunction. For $S = 0$, our calculations lead to the following stationary species I_2, TS2, P_1, P_2 and P_3, as seen in Table 1. Step 3 has a transition state TS2, as can be seen in Fig. 1 and 2, and a single imaginary frequency of $464i$ cm^{-1}.

The energies of the fragments and their corresponding zero point energies are given in Table 1, for each spin state.

We provide in the ESI† the Cartesian coordinates for all fragments involved in the two spin states.

In Table 2 we collect the computed energetics for both total spin states, $S = \{0,1\}$.

In Fig. 2 we plot the relative classical and adiabatic energies of the reaction mechanism under consideration. We see that on the triplet PES, Step 2 can lead to the formation of intermediate I_2 without a barrier to reaction on the UωB97XD/6-311++G(2d,p) vibrationally adiabatic PES while there is a small barrier of 0.43 kcal mol^{-1} using CCSD(T)//UωB97XD, whereas ref. 44 reports a barrier of 5 kcal mol^{-1}.

To balance the computational cost and chemical accuracy, the MEP energies were refined by performing CCSD(T)//UωB97XD/6-311++G(2d,p) single-point energy calculations on the UωB97XD/6-311++G(2d,p) IRC optimized stationary points. The comparison between the MEP energies obtained with the two levels of theory for Steps 2 & 3 can be seen in Fig. 3 and 4.

In Fig. 5 we plot the potential energy, ZPE, and vibrationally adiabatic ground state energy V_a^G along the minimum energy

Table 2 Energetics of the different steps in the reaction mechanism using UωB97XD, and CCSD(T)//UωB97XD/6-311++G(2d,p) level in kcal mol^{-1} for $S = 0$ and 1. Classical barrier height (ΔV), the vibrational adiabatic ground state barrier height (ΔV_a^G), classical ergicity (ΔE) and vibrational adiabatic ergicity (ΔE_a) are shown[a]

Method		UωB97XD				CCSD(T)//UωB97XD			
Reaction steps	Label	ΔV	ΔV_a^G	ΔE	ΔE_a	ΔV	ΔV_a^G	ΔE	ΔE_a
$S = 1$									
RC $\rightarrow$ I_1	Step 1	—	—	−28.61	−28.11	—	—	−20.02	−19.53
I_1 $\rightarrow$ I_2	Step 2	1.727	−1.987	−30.42	−30.91	4.14	0.43	−29.93	−30.42
I_2 $\rightarrow$ P_1	Step 3	16.82	13.78	−5.42	−10.49	16.32	13.28	−8.83	−13.89
P_1 $\rightarrow$ P_2	Step 4	1.94	3.59	−15.63	−11.35	5.34	6.98	−8.29	−4.02
P_1 $\rightarrow$ P_3	Step 4′	29.24	29.81	18.74	22.59	36.44	37.00	24.10	27.95
$S = 0$									
I_2 $\rightarrow$ P_1	Step 3	29.93	24.85	23.46	17.01	28.73	23.55	21.41	14.96
P_1 $\rightarrow$ I_2	Step 3′	6.47	7.84	−23.46	−17.01	13.28	14.65	−21.41	−14.96
P_1 $\rightarrow$ P_2	Step 4	—	—	−90.95	−84.69	—	—	−76.62	−70.36
P_1 $\rightarrow$ P_3	Step 4′	—	—	−85.44	−82.24	—	—	−79.65	−76.45
P_2 $\rightarrow$ Ac(gas) + 7w(cluster)		—	—	9.56	8.17	—	—	9.34	7.95

[a] – indicates barrierless.

path for Step 2. The ZPE variation with respect to the reaction coordinate s exhibits a dip around the transition state, which results in that the 4.14 kcal mol^{-1} classical barrier is reduced to 0.43 kcal mol^{-1}.

Fig. 6 shows the reaction path pertaining to Step 3 on the triplet surface, *i.e.* the energetically rate determining step. The adiabatic barrier height is 13.28 kcal mol^{-1} for this step, which is exothermic. Formation of adsorbed acetaldehyde (Ac) through Step 4 is exothermic by −8.29 kcal mol^{-1} with a moderate vibrationally adiabatic barrier height of 6.98 kcal mol^{-1}. In Fig. 7 we plot, for Step 4 the UωB97XD/6-311++G(2d,p) $V_{MEP}(s)$, $V_a^G(s)$ and ZPE(s) where we clearly see how the variation in ZPE results in an increase of the adiabatic barrier.

The I_2 singlet state has a noticeably lower energy (see Table 1) than the triplet state. We have therefore investigated if a spin flip could happen such that I_2 may form in its singlet state.

We have computed the downhill reaction path starting from the triplet I_2 geometry but with a total spin $S = 0$. We also computed the single point energies for each geometry of this path with total spin $S = 1$. The energies are shown in Fig. 8. The crossing point between the two states is only about 3 kcal mol^{-1}

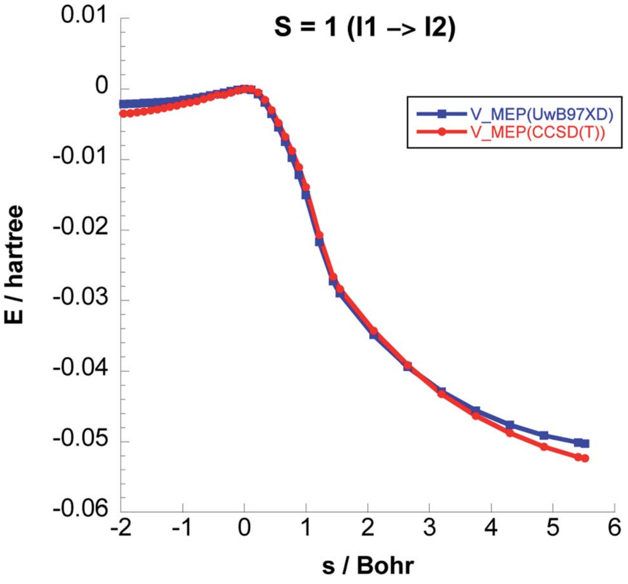

Fig. 3 Comparison between the classical potential energies V_{MEP}, computed with CCSD(T)//UωB97XD/6-311++G(2d,p) and UωB97XD/6-311++G(2d,p) levels, for Step 2 on the $S = 1$ PES.

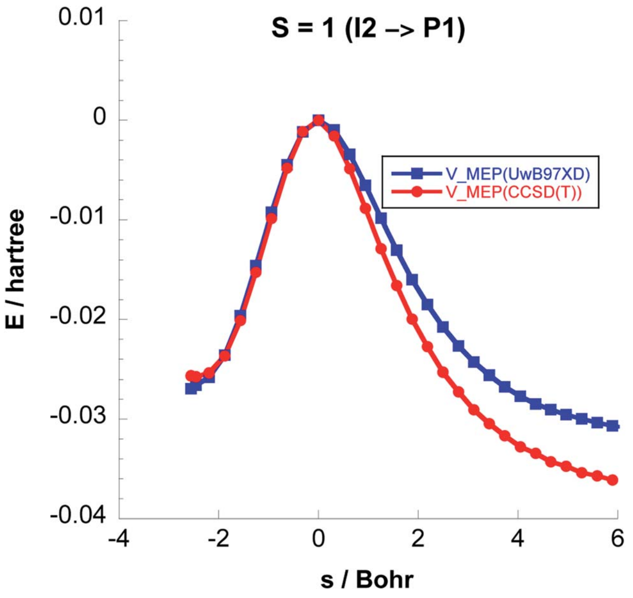

Fig. 4 Comparison between the classical potential energies V_{MEP}, computed with CCSD(T)//UωB97XD/6-311++G(2d,p) and UωB97XD/6-311++G(2d,p) levels, for Step 3 on the $S = 1$ PES.

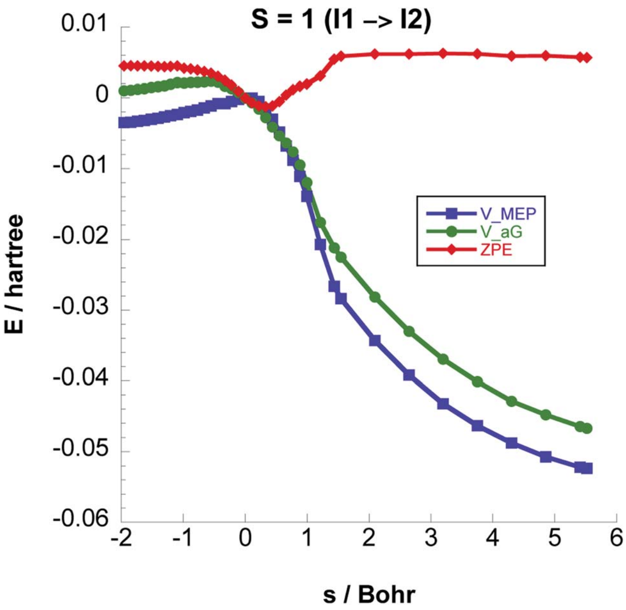

Fig. 5 Classical potential energies V_{MEP}, ground-state vibrational adiabatic potential energy curves (V_a^G), and ZPE as functions of s (Bohr) at the CCSD(T)//UωB97XD/6-311++G(2d,p) level, for Step 2 at a total spin $S = 1$.

above the energy of the triplet I_2 geometry and is thus energetically easily accessible considering the energy released in coming from I_1. The point on the IRC where the energies of triplet and singlet states are the same, indicates a possible intersystem crossing geometry such that I_2 can form as a singlet.

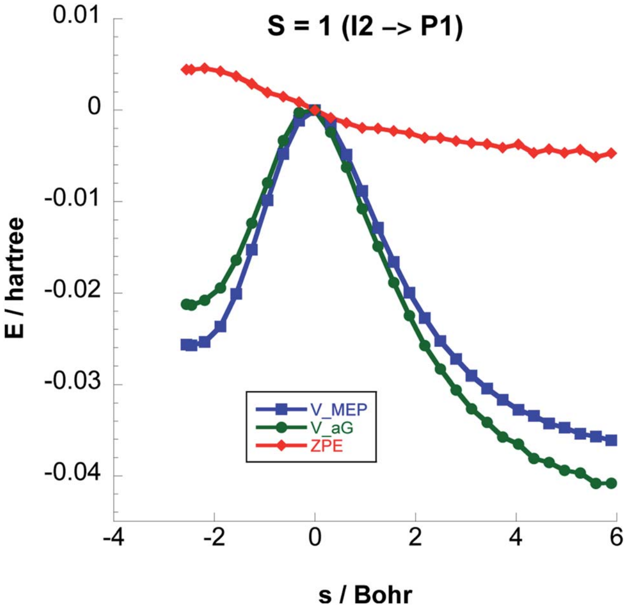

Fig. 6 Classical potential energies V_{MEP}, ground-state vibrational adiabatic potential energy curves (V_a^G), and ZPE as functions of s (Bohr) at the CCSD(T)//UωB97XD/6-311++G(2d,p) level, for Step 3 on the $S = 1$ PES.

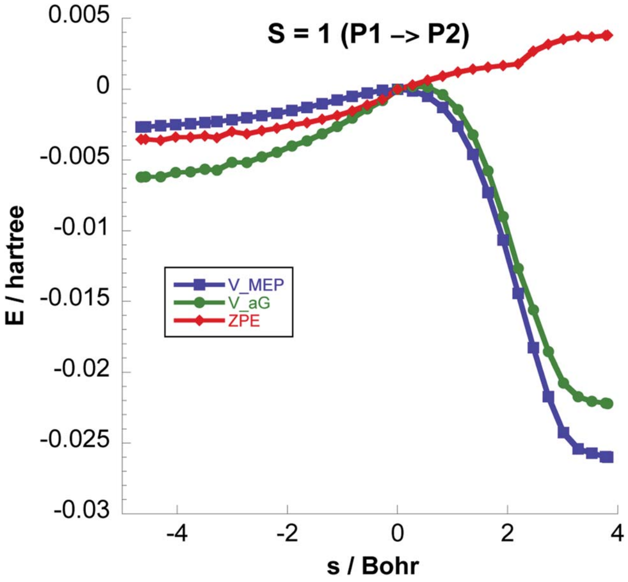

Fig. 7 Classical potential energies V_{MEP}, ground-state vibrational adiabatic potential energy curves (V_a^G), and ZPE of 3N-6 vibrational modes as functions of s (Bohr) at the UωB97XD/6-311++G(2d,p) level, for Step 4 at a total spin $S = 1$.

As a result of a spin flip close to the I_2 intermediate, the next step in order to form acetaldehyde would be I_2 (singlet) → P_1 (singlet) instead of I_2 (triplet) → P_1 (triplet). In Fig. 9 we plot the classical potential energies V_{MEP} from UωB97XD and CCSD(T)//UωB97XD, and also the ZPE for Step 3. The adiabatic barrier height for this step is 23.55 kcal mol^{-1} at the CCSD(T)//UωB97XD level.

The following step to form adsorbed acetaldehyde (step 4) is exoergic by 70.36 kcal mol^{-1}. Desorbtion of acetaldehyde into

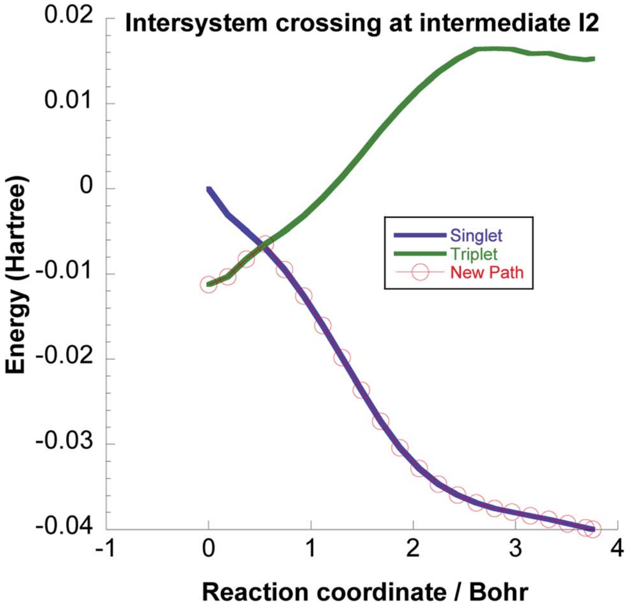

Fig. 8 Intersystem crossing between the triplet and singlet potential energy surfaces at the intermediate I_2.

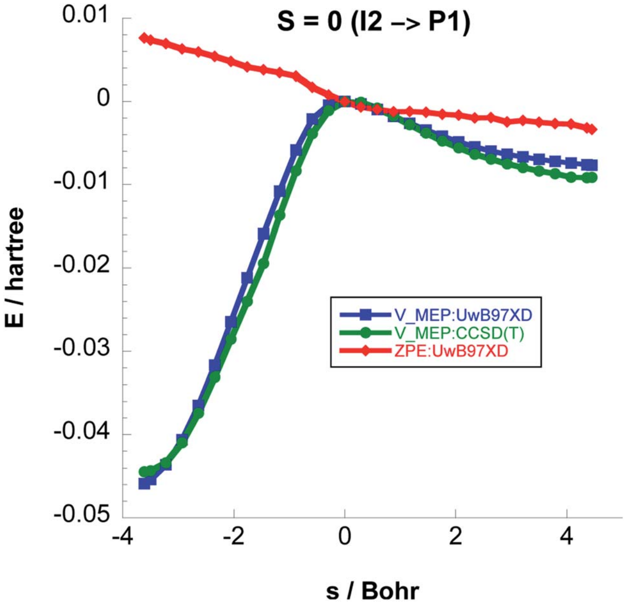

Fig. 9 Classical potential energies V_{MEP}, at the UωB97XD/6-311++G(2d,p) and CCSD(T)//UωB97XD/6-311++G(2d,p) levels of theory, with ZPE as functions of s (Bohr) for Step 3 on the $S = 0$ PES.

the gas phase is endoergic by only 7.95 kcal mol^{-1}, suggesting that the large exoergicity of step 4 would lead to fast desorption.

If there is no spin flip close to I_2, P_1 would form in the triplet state. Again, the singlet P_1 is lower in energy and we have investigated if a spin flip could occur also here, see Fig. 10, which is energetically quite plausible. Thereafter the reaction would proceed on the singlet surface to form adsorbed acetaldehyde which is likely to easily desorb as discussed just above.

For $S = 0$ the $P_1 \rightarrow P_2$ and $P_1 \rightarrow P_3$ reactions are downhill with exoergicities of -70.36 and -76.45 kcal mol^{-1} respectively. For the reactions on the triplet PES, only one unpaired electron (on the CH_3 radical) is involved in either the C–C bond formation (to form P_2) or the H-transfer (to form CH_4), while the other unpaired electron (on HCO-wat radical) stays uninvolved. This is obviously different than the processes on the singlet PES where the two unpaired electrons have opposite spins and they either recombine without barrier for the (C–C) bond formation or transfer an H atom without barrier to lead to two closed shell species. For these reasons on the singlet potential energy surface $P_1 \rightarrow P_2$ (Step 4) and $P_1 \rightarrow P_3$ (Step 4′) are barrierless as can be seen in Fig. 2. Formation of adsorbed CO + CH_4 products (P_3) on the $S = 1$ PES has a barrier of 37 kcal mol^{-1} as can be seen in Table 2.

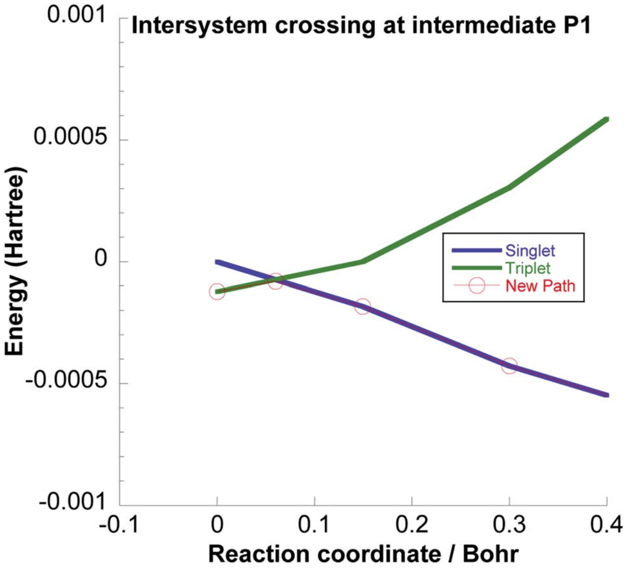

Fig. 10 Intersystem crossing between the triplet and singlet potential energy surfaces at the intermediate P_1.

Table 3 TST, CVT, CVT/ZCT, and CVT/SCT, rate constants in (s^{-1}) for a total spin $S = 1$, for Step 3 ($I_2 \rightarrow P_1$) computed at CCSD(T)//UωB97XD/6-311++G(2d,p) level

T (K)	TST	CVT	CVT/ZCT	CVT/SCT
105	1.19×10^{-15}	5.28×10^{-16}	2.49×10^{-6}	1.19×10^{-5}
120	4.0×10^{-12}	1.78×10^{-12}	6.94×10^{-6}	2.77×10^{-5}
150	3.64×10^{-7}	1.61×10^{-7}	1.64×10^{-4}	3.73×10^{-4}
200	3.63×10^{-2}	1.55×10^{-2}	1.79×10^{-1}	2.20×10^{-1}
300	4.33×10^{3}	1.69×10^{3}	3.32×10^{3}	3.47×10^{3}
400	1.71×10^{6}	6.01×10^{5}	7.35×10^{5}	7.51×10^{5}
500	6.61×10^{7}	2.11×10^{7}	2.14×10^{7}	2.17×10^{7}
600	7.89×10^{8}	2.33×10^{8}	2.16×10^{8}	2.18×10^{8}
700	4.76×10^{9}	1.32×10^{9}	1.16×10^{9}	1.17×10^{9}
800	1.86×10^{10}	4.86×10^{9}	4.13×10^{9}	4.15×10^{9}
900	5.41×10^{10}	1.35×10^{10}	1.12×10^{10}	1.12×10^{10}
1000	1.28×10^{11}	3.07×10^{10}	2.48×10^{10}	2.48×10^{10}
1200	4.72×10^{11}	1.04×10^{11}	7.58×10^{10}	7.59×10^{10}
1400	1.21×10^{12}	2.44×10^{11}	1.62×10^{11}	1.62×10^{11}
1600	2.46×10^{12}	4.55×10^{11}	2.80×10^{11}	2.81×10^{11}
1800	4.27×10^{12}	7.29×10^{11}	4.35×10^{11}	4.35×10^{11}
2000	6.67×10^{12}	1.06×10^{12}	6.29×10^{11}	6.29×10^{11}

Table 4 TST, CVT, CVT/ZCT, and CVT/SCT, rate constants in (s^{-1}) for a total spin $S = 0$, for Step 3 ($I_2 \rightarrow P_1$) computed at CCSD(T)//UωB97XD/6-311++G(2d,p) level

T (K)	TST	CVT	CVT/ZCT	CVT/SCT
107	2.41×10^{-34}	1.13×10^{-34}	3.32×10^{-32}	1.02×10^{-31}
120	3.34×10^{-29}	1.55×10^{-29}	3.04×10^{-28}	4.81×10^{-28}
150	1.06×10^{-20}	4.73×10^{-21}	2.07×10^{-20}	2.23×10^{-20}
200	3.95×10^{-12}	1.63×10^{-12}	3.07×10^{-12}	3.16×10^{-12}
300	2.09×10^{-3}	7.11×10^{-4}	7.60×10^{-4}	7.67×10^{-4}
400	62.3	17.8	15.2	15.2
500	3.48×10^{4}	8.44×10^{3}	6.06×10^{3}	6.07×10^{3}
600	2.56×10^{6}	5.22×10^{5}	3.15×10^{5}	3.16×10^{5}
700	5.76×10^{7}	9.93×106	5.22×10^{6}	5.23×10^{6}
800	6.12×10^{8}	$8.78 \times 10\ 7$	3.35×10^{7}	3.35×10^{7}
900	3.91×10^{9}	4.64×10^{8}	1.67×10^{8}	1.67×10^{8}
1000	1.75×10^{10}	1.74×10^{9}	6.12×10^{8}	6.13×10^{8}
1200	1.68×10^{11}	1.23×10^{10}	4.22×10^{9}	4.23×10^{9}
1400	8.54×10^{11}	4.87×10^{10}	1.73×10^{10}	1.73×10^{10}
1600	2.91×10^{12}	1.35×10^{11}	5.13×10^{10}	5.13×10^{10}
1800	7.60×10^{12}	2.98×10^{11}	1.19×10^{11}	1.19×10^{11}
2000	1.64×10^{13}	5.59×10^{11}	2.35×10^{11}	2.35×10^{11}

Table 5 $k^{CVT/SCT}:k^{CVT/ZCT}$, $k^{TST}:k^{CVT}$, and $k^{CVT/SCT}:k^{CVT}$ ratios for a total spin $S = 1$, for Step 3 ($I_2 \rightarrow P_1$) computed at CCSD(T)//UωB97XD/6-311++G(2d,p) level

T (K)	$k^{CVT/SCT}:k^{CVT/ZCT}$	$k^{TST}:k^{CVT}$	$k^{CVT/SCT}:k^{CVT}$
105	4.7791	2.2538	2.2538×10^{10}
300	1.0452	2.5621	2.0533
500	1.0140	3.1327	1.0284
800	1.0048	3.8272	0.85391
1000	1.0	4.1694	0.80782
1500	1.0	5.1765	0.64118
2000	1.0	6.2925	0.59340

3.2 Rate constants

In this section we report our calculated rate constants for the energetically rate determining step on both the singlet and triplet potential energy surfaces. The thermal rate constants are evaluated by means of canonical variational transition-state theory, *i.e.* CVT, in which the flux is minimized for a canonical ensemble.[64] ZCT and SCT tunneling corrections have been computed for the temperature range 105–2000 K where the fully optimised structures, energies, gradients, and force constants of points along the MEP are provided as inputs. Tables 3 and 4 summarize the TST, CVT, CVT/ZCT, and CVT/SCT, rate constants computed at various temperatures.

The variational effect is defined as the ratio between the TST and CVT rate constants, and the tunneling effect is the ratio between the (CVT/ZCT, CVT/SCT) and CVT rate constants. The ratio between CVT/ZCT and CVT/SCT gives information about the reaction path curvature in the vicinity of the transition state. As such, for Step 3, the CVT/SCT rate constants are predicted to be consistently larger than the CVT/ZCT ones at the same temperature.

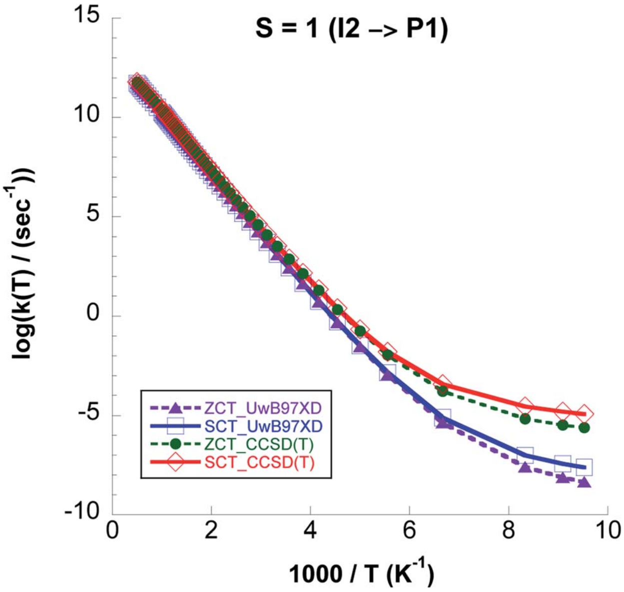

Fig. 12 Logarithm of k(CVT/ZCT) and k(CVT/SCT) rate constants, computed with CCSD(T)//UωB97XD/6-311++G(2d,p) and UωB97XD/6-311++G(2d,p) levels, for Step 3 on the $S = 1$ PES.

In Table 5, we give the calculated ratios of $k^{CVT/SCT}:k^{CVT/ZCT}$, $k^{TST}:k^{CVT}$, and $k^{CVT/SCT}:k^{CVT}$ at some selected temperatures, indicating the importance of the small-curvature, variational and tunneling effects.

Table 5 and Fig. 11 show that tunneling totally dominates at the lowest temperature, but quickly becomes insignificant with increasing temperature, such that reflection by the barrier becomes more important. We also see that the variational effects affect the rate constant, particularly at high temperature.

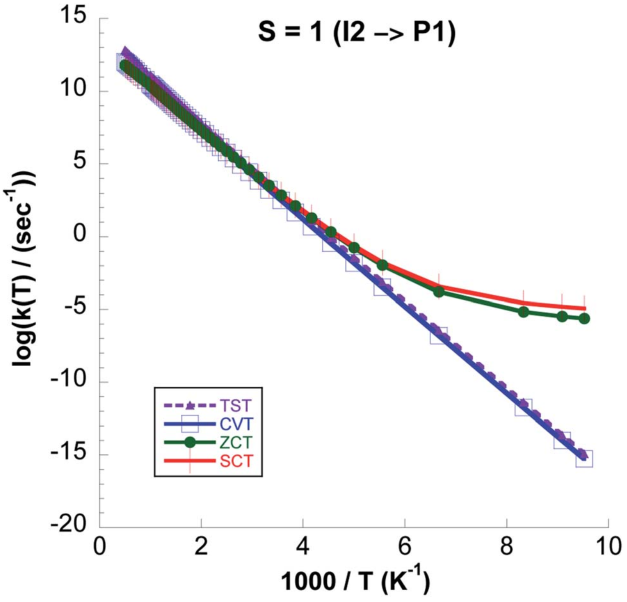

Fig. 11 Logarithmic representation of the k(TST), k(CVT), k(CVT/ZCT) and k(CVT/SCT) rate constants computed at the CCSD(T)//UωB97XD/6-311++G(2d,p) level for the $I_2 \rightarrow P_1$ reaction *versus* 1000/T for $S = 1$.

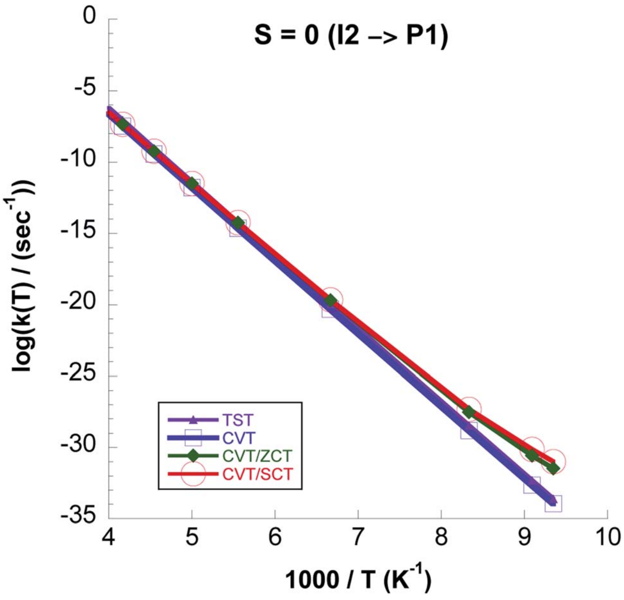

Fig. 13 Logarithmic representation of the k(TST), k(CVT), k(CVT/ZCT) and k(CVT/SCT) rate constants computed at the CCSD(T)//UωB97XD/6-311++G(2d,p) level for the $I_2 \rightarrow P_1$ reaction *versus* 1000/T for $S = 0$.

From Fig. 12 where we compare (CVT/ZCT) and (CVT/SCT) rate constants computed with UωB97XD/6-311++G(2d,p) and CCSD(T)//UωB97XD/6-311++G(2d,p) on the triplet surface we see that the latter model chemistry predicts 4 orders of magnitude higher rate values due to the lower barrier. On the singlet surface, the shape of the reaction path in Fig. 9 shows a broad barrier resulting in only ~3 orders of magnitude difference between the CVT/SCT rates and those from purely classical TST at the lowest temperature.

In Fig. 13 we plot rate constants computed for the $I_2 \rightarrow P_1$ step and total spin $S = 0$. We see that quantum tunneling is only important at temperatures lower than ~130 K. This is also seen from the $k^{CVT/SCT} : k^{CVT}$ ratio in Table 6. Except for the highest temperatures the CVT/SCT rate constants on the $S = 0$ surface are much lower than those on the $S = 1$ PES. From Fig. 14 it is seen that for the whole temperature range CCSD(T)//UωB97XD/6-311++G(2d,p) rate constants are higher than those computed with UωB97XD/6-311++G(2d,p).

Table 6 $k^{CVT/SCT} : k^{CVT/ZCT}$, $k^{TST} : k^{CVT}$, and $k^{CVT/SCT} : k^{CVT}$ ratios for a total spin $S = 0$, for Step 3 ($I_2 \rightarrow P_1$) computed at CCSD(T)//UωB97XD/6-311++G(2d,p) level

T (K)	$k^{CVT/SCT} : k^{CVT/ZCT}$	$k^{TST} : k^{CVT}$	$k^{CVT/SCT} : k^{CVT}$
106	3.1337	2.1298	1.2840×10^3
300	1.0081	2.9478	1.0783
500	1.0020	4.1292	0.71910
800	1.0019	6.9857	0.38286
1000	1.0018	10.0	0.35188
1500	1.0	19.512	0.36856
2000	1.0	29.408	0.42130

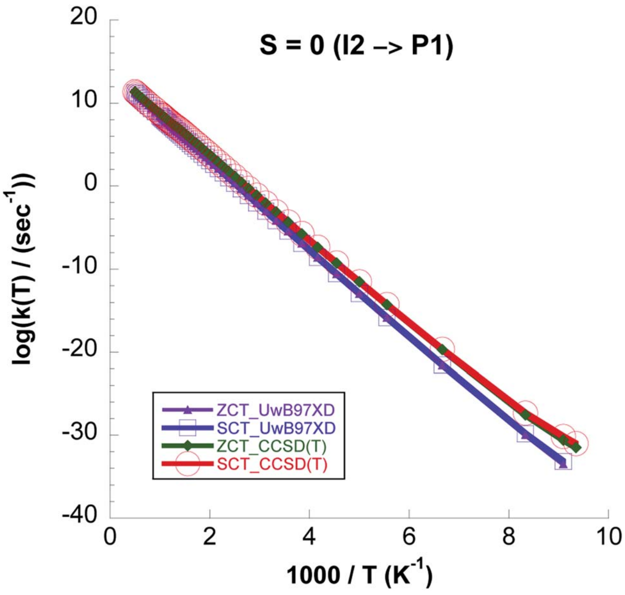

Fig. 14 Comparison between the logarithmic representation of the k(CVT/ZCT) and k(CVT/SCT) rate constants computed with the UωB97XD/6-311++G(2d,p) and the CCSD(T)//UωB97XD/6-311++G(2d,p) level of theory for the $I_2 \rightarrow P_1$ reaction *versus* 1000/T for $S = 0$.

The present work aims to improve the understanding of the reaction mechanisms and kinetics of radical–radical addition on a methanol–water ice model.

The data we provide is of a major interest in regard to astrochemical models. Other molecular species in the ice composition can also be tested in the future, in order to investigate to what extent acetaldehyde formation paths can differ and how the composition of species influences the reaction mechanisms that may change in specific astronomical sources such as cold or hot molecular cores, and star forming regions.

4 Conclusions

We have investigated an Eley-Rideal-type mechanism where $C(^3P)$ reacts with CH_3OH adsorbed on a water cluster. We consider the reaction mechanism on the triplet and the singlet surfaces and discuss two possible intersystem crossings. The reaction begins on the triplet surface and is downhill. It may spin flip close to the first intermediate, *i.e.* between TS1 and TS2. If that happens the reaction continues on the singlet PES, where however the energetically rate limiting step, I_2 to P_1, is much slower than on the triplet surface at interstellar temperatures.

The reaction may on the other hand remain on the triplet surface, pass TS2 and close to P_1 cross to the singlet surface. From P_1 to P_2, *i.e.* to form adsorbed acetaldehyde, the reaction is barrierless and exoergic by 70.36 kcal mol^{-1}. Desorption of the acetaldehyde only requires 8 kcal mol^{-1} and is thus likely to happen fast given the large exoergicity of the previous step. This thus appears to be a plausible route to acetaldehyde formation in the gas phase.

We use transition state theory, with tunnelling corrections, to obtain the thermal rate constants for the energetically rate determining step of the reaction mechanism. In this step adsorbed CH_3OCH breaks up to form adsorbed CH_3 and HCO (on both the triplet and singlet surfaces).

Specifically, variational transition state theory calculations with zero curvature and small tunneling corrections are employed to find thermal rate constants over the temperature range 105–2000 K, relevant to a set of astrophysical environments.

The variational effect is found to be important and have a dominating effect on the obtained rate constants except at the lowest temperature. Tunneling totally dominates the rate constant at the lowest temperature but decreases quickly as the temperature increases. In fact reflection by the barrier clearly dominates over tunneling at the higher temperatures.

We also notice that the zero curvature tunneling correction works just as well as the small curvature correction except at the lowest temperature reported in Tables 5 and 6.

This study may serve as a useful investigation for further model variants to be explored computationally, and to suggest possible constraints on new experimental setups relevant to ice models to gain new impetus in the understanding of COM formation on icy mantles in general.

Conflicts of interest

There are no conflicts to declare.

Acknowledgements

The authors are thankful to Professor D. G. Truhlar for providing the licenses for the Polyrate and Gaussrate programs. The computations were enabled by resources provided by the Swedish National Infrastructure for Computing (SNIC) at Chalmers Centre for Computational Science and Engineering (C3SE) and partially funded by the Swedish Research Council through grant agreement no. 2018-05973. GN is also grateful to the Swedish Research Council for grant 2020-05293 which in part supported this work. BK is very grateful to Gaussian help team for useful insights into the Gaussian computations. IBC expresses her gratitude to Dr Keshav Kumar Singh for providing the Cartesian coordinates of some selected structures.

References

1 J. K. Jorgensen, A. Belloche and R. T. Garrod, *Annu. Rev. Astron. Astrophys.*, 2020, **58**, 727–778.
2 J. Jortner, *Phil. Trans. Biol. Sci.*, 2006, **361**, 1877–1891.
3 E. Herbst and E. Dishoeck, *Annu. Rev. Astron. Astrophys.*, 2009, **47**, 427–480.
4 E. Herbst, *Int. Rev. Phys. Chem.*, 2017, **36**, 287–331.
5 F. Vazart, C. Ceccarelli, N. Balucani, E. Bianchi and D. Skouteris, *Mon. Not. R. Astron. Soc.*, 2020, **499**, 5547–5561.
6 C. J. Bennett, Y. Osamura, M. D. Lebar and R. I. Kaiser, *Astrophys. J.*, 2005, **634**, 698–711.
7 C. J. Bennett, C. S. Jamieson, Y. Osamura and R. I. Kaiser, *Astrophys. J.*, 2005, **624**, 1097–1115.
8 M. Moore and R. Hudson, *Icarus*, 1998, **135**, 518–527.
9 J. E. Hudson, M. L. Hamilton, C. Vallance and P. W. Harland, *Phys. Chem. Chem. Phys.*, 2003, **5**, 3162–3168.
10 A. J. Barnes and H. E. Hallam, *Trans. Faraday Soc.*, 1970, **66**, 1920–1931.
11 V. A. Basiuk and K. Kobayashi, *Int. J. Quantum Chem.*, 2004, **97**, 713–718.
12 E. Herbst, G. Vidali and C. Ceccarelli, *ACS Earth Space Chem.*, 2020, **4**, 488–490.
13 K.-J. Chuang, G. Fedoseev, D. Qasim, S. Ioppolo, E. van Dishoeck and H. Linnartz, *Mon. Not. R. Astron. Soc.*, 2017, **467**, 2552–2565.
14 A. Ciaravella, A. Jiménez-Escobar, G. Cosentino, C. Cecchi-Pestellini, G. Peres, R. Candia, A. Collura, M. Barbera, G. D. Cicca, S. Varisco and A. M. Venezia, *Astrophys. J.*, 2018, **858**, 35.
15 K.-J. Chuang, G. Fedoseev, D. Qasim, S. Ioppolo, C. Jäger, Th. Henning, M. E. Palumbo, E. F. van Dishoeck and H. Linnartz, *Astron. Astrophys.*, 2020, **635**, A199.
16 C. A. Gottlieb, *Detection of Acetaldehyde in Sagittarius. Molecules in the Galactic Environment*, 1973, p. 181.
17 N. Fourikis, M. W. Sinclair, B. J. Robinson, P. D. Godfrey and R. D. Brown, *Aust. J. Phys.*, 1974, **27**(3), 425–430.
18 A. Bacmann, V. Taquet, A. Faure, C. Kahane and C. Ceccarelli, *Astron. Astrophys.*, 2012, **541**, L12.
19 J. Cernicharo, N. Marcelino, E. Roueff, M. Gerin, A. Jiménez-Escobar and G. M. M. Caro, *Astrophys. J.*, 2012, **759**, L43.
20 V. Taquet, E. S. Wirström, S. B. Charnley, A. Faure, A. López-Sepulcre and C. M. Persson, *Astron. Astrophys.*, 2017, **607**, A20.
21 B. E. Turner, R. Terzieva and E. Herbst, *Astrophys. J.*, 1999, **518**, 699–732.
22 A. Bacmann, A. Faure and J. Berteaud, *ACS Earth Space Chem.*, 2019, **3**, 1000–1013.
23 J. Crovisier, D. Bockelée-Morvan, N. Biver, P. Colom, D. Despois and D. C. Lis, *Astron. Astrophys.*, 2004, **418**, L35–L38.
24 R. T. Garrod and E. Herbst, *Astron. Astrophys.*, 2006, **457**, 927–936.
25 G. Jungclaus, G. Yuen, C. Moore and J. Lawless, *Meteoritics*, 1976, **11**, 231–237.
26 P. Clarke, D. Smith, A. Steer and N. Bia, *Chem. Commun.*, 2017, **53**, 10362–10365, © 2017, The Royal Society of Chemistry. This is an author-produced version of the published paper. Uploaded in accordance with the publisher's self-archiving policy. Further copying may not be permitted; contact the publisher for details.
27 H. J. Cleaves II, *Monatsh. Chem.*, 2003, **134**, 585–593.
28 A. Hjalmarson, P. Bergman and A. Nummelin, *1st European Workshop on Exo-/astro-biology*, 2001, p. 263.
29 S. Charnley, A. Tielens and T. Millar, *Astrophys. J.*, 1992, **399**, L71.
30 S. Charnley, *Adv. Space Res.*, 2004, **33**, 23–30.
31 J. Enrique-Romero, A. Rimola, C. Ceccarelli and N. Balucani, *Mon. Not. Roy. Astron. Soc. Lett.*, 2016, **459**, L6–L10.
32 J. Enrique-Romero, A. Rimola, C. Ceccarelli, P. Ugliengo, N. Balucani and D. Skouteris, *ACS Earth Space Chem.*, 2019, **3**, 2158–2170.
33 J. Enrique-Romero, S. Alvarez-Barcia, F. J. Kolb, A. Rimola, C. Ceccarelli, N. Balucani, J. Meisner, P. Ugliengo, T. Lamberts and J. Kastner, *Mon. Not. R. Astron. Soc.*, 2020, **493**, 2523–2527.
34 S. Maity, R. I. Kaiser and B. M. Jones, *Phys. Chem. Chem. Phys.*, 2015, **17**, 3081–3114.
35 M. J. Abplanalp, S. Gozem, A. I. Krylov, C. N. Shingledecker, E. Herbst and R. I. Kaiser, *Mon. Not. Roy. Astron. Soc. Lett.*, 2016, **113**, 7727–7732.
36 T. Lamberts, M. N. Markmeyer, F. J. Kolb and J. Kastner, *ACS Earth Space Chem.*, 2019, **3**, 958–963.
37 V. Wakelam, *et al.*, *Astrophys. J. Suppl.*, 2012, **199**, 21.
38 D. McElroy, C. Walsh, A. J. Markwick, M. A. Cordiner, K. Smith and T. J. Millar, *Astron. Astrophys.*, 2013, **550**, A36.
39 M. J. Abplanalp and R. I. Kaiser, *Phys. Chem. Chem. Phys.*, 2019, **21**, 16949–16980.
40 K. I. Öberg, R. T. Garrod, E. F. van Dishoeck and H. Linnartz, *Astron. Astrophys.*, 2009, **504**, 891–913.
41 R. Martín-Doménech, G. M. Muñoz Caro and G. A. Cruz-Díaz, *Astron. Astrophys.*, 2016, **589**, A107.
42 N. F. Kleimeier, A. M. Turner, R. C. Fortenberry and R. I. Kaiser, *ChemPhysChem*, 2020, **21**, 1531–1540.

43 R. L. Hudson and M. H. Moore, *Astrophys. J.*, 2018, **857**, 89.

44 K. K. Singh, P. Tandon and A. Misra, Formation of Acetaldehyde in the Interstellar Medium from the Reaction of Methanol and Atomic Carbon in Interstellar Water Ice, *Advances in Spectroscopy: Molecules to Materials*, Singapore, 2019, pp. 415–422.

45 P. Hohenberg and W. Kohn, *Phys. Rev.*, 1964, **136**, B864–B871.

46 K. Raghavachari, G. W. Trucks, J. A. Pople and M. Head-Gordon, *Chem. Phys. Lett.*, 1989, **157**, 479–483.

47 M. J. Frisch *et al.*, *Gaussian 16 Revision C.01*, Gaussian Inc, Wallingford CT, 2016.

48 J.-D. Chai and M. Head-Gordon, *Phys. Chem. Chem. Phys.*, 2008, **10**, 6615–6620.

49 J. M. L. Martin, J. P. François and R. Gijbels, *J. Comput. Chem.*, 1989, **10**, 875–886.

50 D. K. Singh, S. Cha, D. Nam, H. Cheong, S.-W. Joo and D. Kim, *ChemPhysChem*, 2016, **17**, 3040–3046.

51 D. K. Singh, B. Rathke, J. Kiefer and A. Materny, *J. Phys. Chem.*, 2016, **120**, 6274–6286.

52 H. P. Hratchian and H. B. Schlegel, *J. Chem. Phys.*, 2004, **120**, 9918–9924.

53 H. P. Hratchian and H. B. Schlegel, *J. Chem. Theory Comput.*, 2005, **1**, 61–69.

54 J. Zheng *et al.*, *Polyrate-version 2017-C*, University of Minnesota, Minneapolis, 2017.

55 D. G. Truhlar and B. C. Garrett, *Acc. Chem. Res.*, 1980, **13**, 440–448.

56 Y. P. Liu, G. C. Lynch, T. N. Truong, D. H. Lu, D. G. Truhlar and B. C. Garrett, *J. Am. Chem. Soc.*, 1993, **115**, 2408–2415.

57 R. T. Skodje, D. G. Truhlar and B. C. Garrett, *J. Phys. Chem.*, 1981, **85**, 3019–3023.

58 A. G. Vandeputte, M. K. Sabbe, M.-F. Reyniers, V. Van Speybroeck, M. Waroquier and G. B. Marin, *J. Phys. Chem.*, 2007, **111**, 11771–11786.

59 M. A. Ali, *Sci. Rep.*, 2020, **10**, 10995–11008.

60 M. Akbar Ali, M. Balaganesh and K. C. Lin, *Phys. Chem. Chem. Phys.*, 2018, **20**, 4297–4307.

61 M. A. Ali, M. Balaganesh and S. Jang, *Atmos. Environ.*, 2019, **207**, 82–92.

62 A. Parandaman, C. B. Tangtartharakul, M. Kumar, J. S. Francisco and A. Sinha, *J. Phys. Chem.*, 2017, **121**, 8465–8473.

63 I. Oueslati, B. Kerkeni, A. Spielfiedel, W.-L. Tchang-Brillet and N. Feautrier, *J. Phys. Chem.*, 2014, **118**, 791–802.

64 N. Henriksen and F. Hansen, *Theories of molecular reaction dynamics: the microscopic foundation of chemical kinetics*, Oxford University Press, United States, 1st edn, Oxford graduate texts, 2008.